

Subsurface Characterization using Ensemble-based Approaches with Deep Generative Models

Jichao Bao¹, Hongkyu Yoon², and Jonghyun Lee¹

¹University of Hawaii at Manoa, Honolulu, HI, USA

²Sandia National Laboratories, Albuquerque, NM, USA

Key Points:

- Subsurface characterization using the Wasserstein generative adversarial network with gradient penalty.
- Gaussian, channelized, and fractured fields are tested to demonstrate the accuracy and efficiency of our approach.
- The ensemble-based and optimization-based approaches are compared to demonstrate why the ensemble-based approach performs better with GANs.

arXiv:2310.00839v1 [cs.LG] 2 Oct 2023

Abstract

Estimating spatially distributed properties such as hydraulic conductivity (K) from available sparse measurements is a great challenge in subsurface characterization. However, the use of inverse modeling is limited for ill-posed, high-dimensional applications due to computational costs and poor prediction accuracy with sparse datasets. In this paper, we combine Wasserstein Generative Adversarial Network with Gradient Penalty (WGAN-GP), a deep generative model that can accurately capture complex subsurface structure, and Ensemble Smoother with Multiple Data Assimilation (ES-MDA), an ensemble-based inversion method, for accurate and accelerated subsurface characterization. WGAN-GP are trained to generate high-dimensional K fields from a low-dimensional latent space and ES-MDA then updates the latent variables by assimilating available measurements. Several subsurface examples are used to evaluate the accuracy and efficiency of the proposed method and the main features of the unknown K fields are characterized accurately with reliable uncertainty quantification.

Furthermore, the estimation performance is compared with a widely-used variational, i.e., optimization-based, inversion approach, and the proposed approach outperforms the variational inversion method, especially for the channelized and fractured field examples. We explain such superior performance by visualizing the objective function in the latent space: because of nonlinear and aggressive dimension reduction via generative modeling, the objective function surface becomes extremely complex while the ensemble approximation can smooth out the multi-modal surface during the minimization. This suggests that the ensemble-based approach works well over the variational approach when combined with deep generative models at the cost of forward model runs unless convergence-ensuring modifications are implemented in the variational inversion.

1 Introduction

Subsurface characterization is critical for subsurface energy storage and recovery processes and risk management associated with subsurface reservoir activities (Tartakovsky, 2013; Newell et al., 2017; Kang et al., 2020, 2021; Ghorbanidehno et al., 2020; Yoon et al., 2013). However, heterogeneous aquifer properties such as hydraulic conductivity is a great challenge for subsurface characterization because of the limited number of observations and uncertainty in numerical models. Data assimilation (DA) approach offers a solution to integrate dynamic data (e.g., time-series pressure) into numerical models, identify unknown model parameters, and reduce the estimation uncertainty (Y. Liu & Gupta, 2007; Y. Liu et al., 2012). Among various DA methods, Kalman-type methods are widely used for their optimality and efficiency for linear-Gaussian problems while code-intrusive implementation of the adjoint state method and successive linearizations are required for nonlinear, non-Gaussian applications (Carrassi et al., 2018). The ensemble Kalman filter (EnKF) (Evensen, 1994) is one of the most popular Kalman-type methods for its simplicity and easy implementation without intrusive code changes. For example, Chen and Zhang (2006) applied EnKF to continuously update hydraulic conductivity and hydraulic head by assimilating dynamic and static data. The results demonstrated that the estimated conductivity field using EnKF matches the reference field very well. Moreover, incorrect prior knowledge can be rectified to some extent through DA procedure. G. Liu et al. (2008) implemented EnKF to investigate the flow and transport processes at the macro-dispersion experiment (MADE) site in Columbus, Mississippi, USA. The advection-dispersion (AD) model and the dual-domain mass transfer (DDMT) model were used to analyze the tritium plume. Piezometric head measurements and tritium concentrations were assimilated to estimate the hydraulic conductivity and major parameters of the AD and DDMT models such as dispersion coefficients and mass transfer rates. This work demonstrated that EnKF is an efficient method for solving large-scale, nonlinear fluid flow and transport problems. Li et al. (2012) applied EnKF to jointly estimate hydraulic conductivity and porosity by assimilating hydraulic head and con-

centration data. The results also showed that integrating more and different types of data could improve predictions of groundwater flow and solute transport.

One disadvantage of EnKF is that the update process requires repeated parameter estimation and restarting the simulation at each time step, which is time-consuming and difficult to implement when multiphysics models are involved (Zhang et al., 2018). Various methods have been proposed to address the challenges, and ensemble smoother (ES) (Van Leeuwen & Evensen, 1996) is an alternative to EnKF. All the data are simultaneously assimilated through ES, which significantly reduces the computational burden. However, the data are used only once through ES, i.e., ensemble Kalman update is performed only once in each iteration, to achieve a global update, which might not be able to produce acceptable results due to premature convergence to the optimal estimate. Therefore, some iterative methods have been proposed (Gu & Oliver, 2007; Chen & Oliver, 2012). Ensemble smoother with multiple data assimilation (ES-MDA) (A. A. Emerick & Reynolds, 2013) is one of the most promising approaches. The observed data can be used multiple times by ES-MDA and iteratively integrated into the models, i.e., Kalman update is corrected through iterative linearizations in each iteration, to achieve a better result. Tavakoli et al. (2013) and A. A. Emerick (2016) investigated the performance of ES-MDA in history matching of production and seismic data as well as CO₂ saturation in geologic carbon storage. The results showed that ES-MDA can produce plausible estimates of reservoir properties with a reasonable match to the observed production data. Fokker et al. (2016) implemented ES-MDA to estimate the subsurface model parameters of the Bergermeer gas field. The line-of-sight measurements were used in the DA process and ES-MDA yielded reasonable estimates of the compaction coefficient and elastic modulus.

The Kalman-type, which is considered as linear(ized)-Gaussian, methods share a common problem, i.e., the limitation of Gaussian assumption (Ghorbanidehno et al., 2020). These Gaussian prior-based methods can provide optimal solutions if the prior follows a multi-Gaussian distribution, but there are also many non-Gaussian situations such as channelized aquifers that these methods cannot handle (Zhou et al., 2014). Although a variety of approaches such as power transformation from non-Gaussian to Gaussian prior or Monte Carlo sampling have been proposed to deal with the non-Gaussian cases (e.g., Oliver et al., 1997; Hu, 2000; Le et al., 2015), the heavy computational burden may hinder the application of these methods. Moreover, DA and inverse models even with the Gaussian prior are prohibited by high-dimensional problems with expensive forward models unless one considers fast linear algebra (Wang et al., 2021), dimension reduction (Lee & Kitanidis, 2014; Ghorbanidehno et al., 2020), and/or reduced order modeling (Kadeethum et al., 2021). In recent decades, the fast growth of deep learning (DL) and its impressive applications in many fields provide a new direction to address these non-Gaussian estimations and computationally challenging issues in the DA. Specifically, deep generative models (Goodfellow et al., 2014) have attracted significant attention due to their promising ability to represent data distributions and generate new samples in an efficient and accurate fashion. Deep generative models can be used for different tasks such as generating synthetic but realistic images, enhancing image resolution, and recovering missing parts of data (Turhan & Bilge, 2018).

Among many deep generative models, generative adversarial network (GAN) (Goodfellow et al., 2014) has become one of the widely used generative models in DA because of its capability to sample from the target distribution. GAN includes a generator and a discriminator. The generator converts randomly sampled latent variables into generated data, and the discriminator determines whether the data are authentic (Grover et al., 2018). Several attempts to apply GAN in the subsurface systems have been conducted. Sun (2018) presented a state-parameter identification GAN (SPID-GAN) to learn the bidirectional mappings between the high-dimensional parameter space and the corresponding model state space. Groundwater flow modeling was conducted and the results demonstrated

that SPID-GAN performed well in approximating the bidirectional state-parameter mappings. Laloy et al. (2018) introduced a spatial GAN (SGAN) to generate high-dimensional complex media samples. 2D steady-state flow and 3D transient hydraulic tomography cases were presented to show the performance of SGAN-based inversion approach. The results illustrated that the SGAN-based approach can produce earth model realizations that are similar to the true model and fit the data well. Janssens et al. (2020) applied GAN to improve the resolution of computed tomography (CT) scans. The results showed that the GAN-based super-resolution method can better characterize the pore networks and fluid flow properties. Using the improved super-resolution CT scans as input resulted in more accurate simulations. Patel and Oberai (2021) used GAN-based prior to solve Bayesian inverse problems in a Monte Carlo framework and one of their applications is to estimate the permeability field.

Despite the impressive applications, the drawbacks of naïve GAN are mode collapse and training instability. Mode collapse is the generator collapsing to generate only one or a small subset of different outputs or modes. The Hessian of the loss function in a GAN is indefinite, so the optimal solution is therefore to find a saddle point instead of a local minimum. The stochastic gradient methods commonly used for training cannot reliably converge to a saddle point, and converging to a saddle point requires good initialization, which leads to training instability (Creswell et al., 2018). To address these issues, variants of GAN have been proposed (e.g., Nowozin et al., 2016; Mao et al., 2017; Zhao et al., 2016; Berthelot et al., 2017). Arjovsky et al. (2017) introduced the Wasserstein GAN (WGAN) with a new metric called earth-mover (or Wasserstein-1) distance to measure the distance between the generated distribution and real distribution. The weight clipping strategy was used in the original WGAN implementation. However, Gulrajani et al. (2017) found that simply clipping the weights might limit the ability of the discriminator, and they provided another solution called gradient penalty. This new variant of GAN was named WGAN-GP, in which the norm of discriminator gradients with respect to data samples was penalized during training. The results showed that WGAN-GP could stabilize the training process and alleviate the mode collapse problem (Kadeethum et al., 2022). Furthermore, it is expected that the gradient of WGAN-GP is more regular than that of “vanilla” GAN so that the data assimilation techniques based on gradient evaluation of the objective function would benefit and converge to the optimal solution with a smaller number of iterations.

While WGAN-GP has shown better performance in complex image generation, it has rarely been used for subsurface DA or inverse problems. In this paper, we will propose a WGAN-GP and ES-MDA based subsurface characterization approach and apply it to several inverse modeling examples (Gaussian, channelized, and fractured aquifers) to show the performance of our proposed method. Based on our applications, we will show the highly non-linear objective function surface of the data assimilation problem when used with GAN, which is a side product of the aggressive data dimension reduction via GAN, and experimentally show that ensemble-based methods would be better performed than the variational, i.e., optimization-based, inverse modeling approach at the cost of more forward model runs, which will be our additional contribution of this paper. The rest of this paper is organized as follows: the methodology is introduced in Section 2. Synthetic applications are shown in Section 3, and some discussions on the benefit of ensemble-based approaches are presented in Section 4. Finally, conclusions are summarized in Section 5.

2 Methodology

2.1 Wasserstein Generative Adversarial Network with Gradient Penalty

2.1.1 Background

The training strategy of GAN can be defined as a minimax game between two competing networks, i.e., a generator network and a discriminator network (Goodfellow et al., 2014):

$$\min_G \max_D E_{x \sim P_x} [\log D(x)] + E_{\mathbf{z} \sim P_z} [\log(1 - D(G(\mathbf{z})))] \quad (1)$$

where x represents the training data and P_x is the data distribution; $G(\mathbf{z})$ represents the generated samples ($G(\mathbf{z}) = \tilde{x} \sim P_g$, and P_g is the generator distribution); \mathbf{z} represents the latent space variables sampled from a simple distribution P_z such as a Gaussian distribution; G is the generator network that maps the input variables \mathbf{z} to the data space, and D is the discriminator network that evaluates the probability that the data comes from the data distribution P_x or the generator distribution P_g . During training, the discriminator attempts to assign correct labels to both training data and samples from P_g while the generator tries to fool the discriminator. Through this interactive process, the generator G learns a distribution P_g that is close to the data distribution P_x .

However, commonly used metrics in GAN such as Kullback-Leibler (KL) divergence and Jensen-Shannon (JS) (Goodfellow et al., 2014) may not be continuous with respect to the generator’s parameters, which makes training difficult. Therefore, Arjovsky et al. (2017) proposed to use the so-called earth-mover (or Wasserstein-1) distance $W(P_x, P_g)$ as an alternative:

$$W(P_x, P_g) = \inf_{\gamma \in \Pi(P_x, P_g)} E_{(x,y) \sim \gamma} [\|x - y\|] \quad (2)$$

where $\Pi(P_x, P_g)$ represents all joint distributions $\gamma(x, y)$ whose marginal distributions are P_x and P_g respectively. The earth-mover (EM) distance is the minimum cost of moving “mass” from x to y in order to transform the distribution P_x into P_g .

Under mild assumptions, the EM distance $W(P_x, P_g)$ is continuous everywhere and differentiable almost everywhere (Arjovsky et al., 2017). The loss function in Wasserstein GAN (WGAN) is defined using the Kantorovich-Rubinstein duality (Villani, 2009) as follows:

$$\min_G \max_{D \in \mathcal{D}} E_{x \sim P_x} [D(x)] + E_{\mathbf{z} \sim P_z} [D(G(\mathbf{z}))] \quad (3)$$

where \mathcal{D} is a set of 1-Lipschitz functions, i.e., discriminator whose rate of change is bounded by a constant (=1) (O’Searcoid, 2006). The discriminator D in WGAN is called a “critic” since it is a real-valued function rather than a classifier, but we will still use the word “discriminator” to keep it consistent with the existing GAN structure. Arjovsky et al. (2017) proposed a weight clipping strategy to constrain the weights in a compact space $[-c, c]$ (e.g., $[-0.01, 0.01]$) to enforce the Lipschitz continuity. However, the weight clipping might limit the networks’ capabilities and cause gradient vanishing or exploding during training. Gulrajani et al. (2017) introduced an alternative way to enforce the Lipschitz constraint called the gradient penalty in which the discriminator loss is defined as:

$$L_D = \underbrace{E_{\mathbf{z} \sim P_z} [D(G(\mathbf{z}))] - E_{x \sim P_x} [D(x)]}_{\text{original discriminator loss}} + \underbrace{\lambda E_{\hat{x} \sim P_{\hat{x}}} [(\|\nabla_{\hat{x}} D(\hat{x})\|_2 - 1)^2]}_{\text{gradient penalty}} \quad (4)$$

where the random samples $\hat{x} \sim P_{\hat{x}}$ land on the straight lines between pairs of points sampled from the data distribution P_x and the generator distribution P_g (Figure 1 (a)). Enforcing the gradient constraint everywhere is intractable, but enforcing it only along the straight lines would be sufficient for the Lipschitz condition and can lead to good training performance. The factor λ is set to 10 as suggested in their paper (Gulrajani et al., 2017).

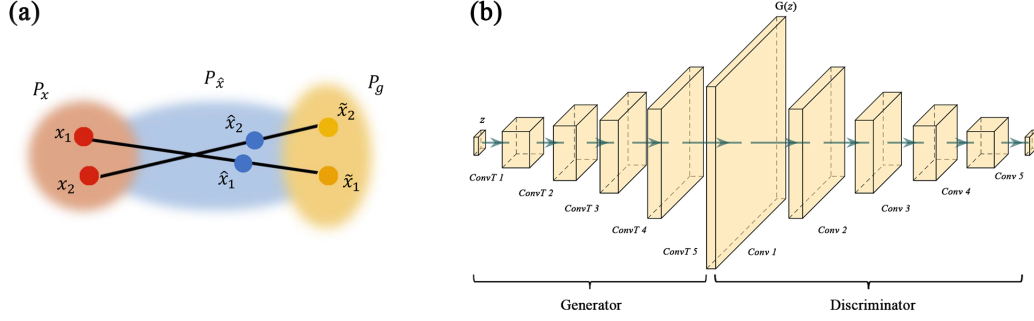


Figure 1. (a) Schematic diagram of gradient penalty. The red area represents the data distribution P_x , the yellow area represents the generator distribution P_g , and the blue area represents the penalty distribution $P_{\hat{x}}$. $\hat{x}_i \sim P_{\hat{x}}$ indicates random samples from the straight lines connecting x_i and \tilde{x}_i ($x_i \sim P_x$, and $\tilde{x}_i \sim P_g$). (b) The architecture of WGAN-GP. \mathbf{z} represents the latent space variables, $G(\mathbf{z})$ indicates the images generated by the generator G , $ConvT$ is the transposed convolutional layer, and $Conv$ represents the convolutional layer.

2.1.2 Training

The architecture of WGAN with gradient penalty (WGAN-GP) used in this paper is illustrated in Figure 1 (b). Two training sessions were performed using a Gaussian (log-normal) hydraulic conductivity field dataset shown in Figure 2 (a) and a channelized binary field dataset shown in Figure 2 (b). The trained generators were then applied to synthetic data assimilation experiments. Each dataset contains 80,000 images and the size of each image is 96×96 . Gaussian training images were generated by the sequential Gaussian simulation (Gómez-Hernández & Journel, 1993) using SGeMS software (Remy et al., 2009). The images were produced using simple Kriging with a spherical variogram. The nugget effect is 0 and the contribution is 1. The search ellipsoid has ranges of 60 and 40 with 0 azimuth. The values were normalized to $[0, 1]$ for the training purpose as in Figure 2 (a). For channelized aquifer characterization case, 80,000 training images (size 96×96) were randomly chosen from the 2500 x 2500 multi-point geostatistical training image (Laloy et al., 2018) as shown in Figure 2 (b).

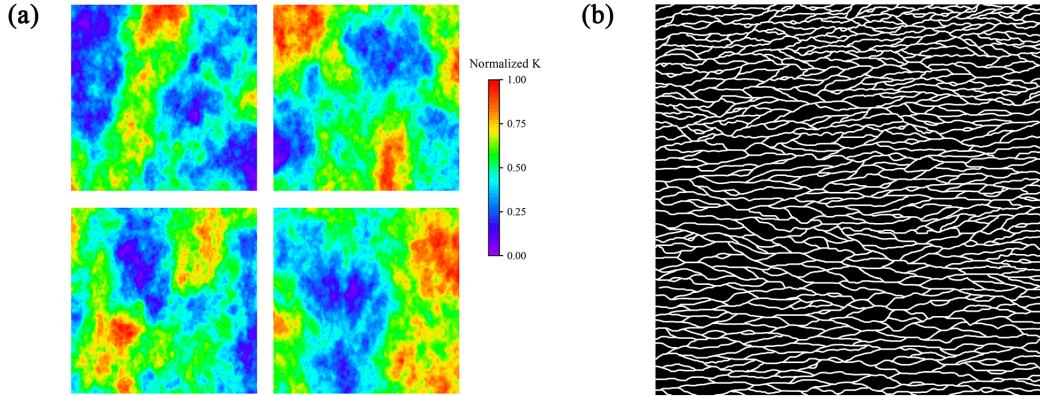


Figure 2. (a) Examples of Gaussian training images. (b) Channelized subsurface training image (2500×2500) from (Laloy et al., 2018).

The details of network parameters for the Gaussian field dataset are shown in Table 1. In the table, k represents the kernel size, s represents the stride, p represents the zero-paddings, d represents the dilation, and InsNorm2d represents the instance normalization. The generator was trained with two-dimensional transposed convolutional layer (ConvT2d). The activation function of the first 3 layers was ReLU, and the final layer was a Sigmoid function. The discriminator was trained using 2D convolutional layers (Conv2d). The activation functions of the first 3 layers were LeakyReLU(0.2), and there was no activation function for the final layer. The latent space z was set to 6×6 . For the channelized dataset the network parameters are shown in Table 2. With hyperparameter optimization adding one more layer to the generator and the discriminator of the deep learning model for the Gaussian field resulted in a better result for the channelized data with the latent space dimension z set to 3×3 . All models were constructed using PyTorch (Paszke et al., 2019).

Table 1. The generator and discriminator architectures for Gaussian data

Generator	Discriminator
Input: 6×6 latent space \mathbf{z}	Input: 96×96 image
Layer 1: ConvT2d, 4k 2s 1p 1d, InsNorm2d, ReLU	Layer 1: Conv2d, 4k 2s 1p 1d, InsNorm2d, LeakyReLU
Layer 2: ConvT2d, 4k 2s 1p 1d, InsNorm2d, ReLU	Layer 2: Conv2d, 4k 2s 1p 1d, InsNorm2d, LeakyReLU
Layer 3: ConvT2d, 4k 2s 1p 1d, InsNorm2d, ReLU	Layer 3: Conv2d, 4k 2s 1p 1d, InsNorm2d, LeakyReLU
Layer 4: ConvT2d, 4k 2s 1p 1d, Sigmoid	Layer 4: Conv2d, 4k 2s 1p 1d
Output: 96×96 image	Output: 6×6 array

Table 2. The generator and discriminator architectures for channelized data

Generator	Discriminator
Input: 3×3 latent space \mathbf{z}	Input: 96×96 image
Layer 1: ConvT2d, 4k 2s 1p 1d, InsNorm2d, ReLU	Layer 1: Conv2d, 4k 2s 1p 1d, InsNorm2d, LeakyReLU
Layer 2: ConvT2d, 4k 2s 1p 1d, InsNorm2d, ReLU	Layer 2: Conv2d, 4k 2s 1p 1d, InsNorm2d, LeakyReLU
Layer 3: ConvT2d, 4k 2s 1p 1d, InsNorm2d, ReLU	Layer 3: Conv2d, 4k 2s 1p 1d, InsNorm2d, LeakyReLU
Layer 4: ConvT2d, 4k 2s 1p 1d, InsNorm2d, ReLU	Layer 4: Conv2d, 4k 2s 1p 1d, InsNorm2d, LeakyReLU
Layer 5: ConvT2d, 4k 2s 1p 1d, Sigmoid	Layer 5: Conv2d, 4k 2s 1p 1d
Output: 96×96 image	Output: 3×3 array

The training process was conducted using an NVIDIA TITAN V GPU card. The training for the Gaussian dataset took 2.5 hours with 60 epochs. The training for the

channelized dataset took 3.3 hours with 50 epochs. The batch size and learning rate were set to 32 and 1e-4, respectively.

Residual networks (ResNets) (He et al., 2016) were used as the classifier/discriminator and they were trained with the real samples from Figure 2 and samples generated by the pre-trained generators. The real samples were labeled as “1” and the generated samples were labeled as “0”. The architecture of the ResNet-based discriminator is shown in Figure 3. To evaluate the performance of the trained generator, we performed the nearest neighbor sample test (Lopez-Paz & Oquab, 2016; Xu et al., 2018) where the generated samples were classified with the same label as their nearest neighbors. If the generator distribution is the same as the data distribution ($P_g = P_r$), generated samples should have an equal probability of being classified as real data or generated data, then classification becomes like the random guess. Consequently, the nearest neighbor sample test should yield around 50% accuracy when $P_g = P_r$. The details about the nearest neighbor sample tests and efficient calculation can be found in (Xu et al., 2018). The nearest neighbor sample tests were performed by using 2,000 unlabeled images from the training datasets and 2,000 unlabeled images generated by the trained generators stored over the entire training epochs.

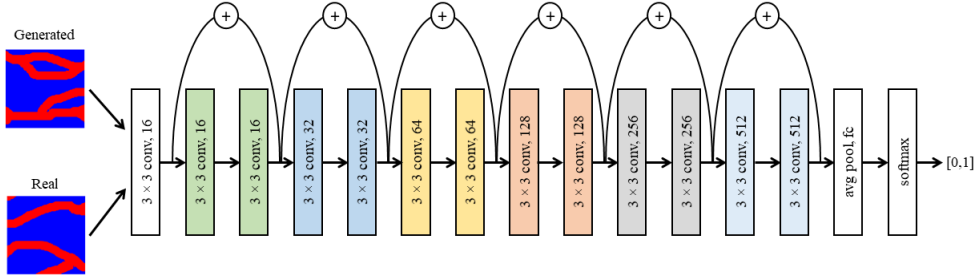


Figure 3. The architecture of ResNet. The residual blocks are marked with different colors. “3×3 conv, 16” represents the convolutional layer with 3×3 kernel and the output has 16 channels. “avg pool” represents the average pooling layer, “fc” represents the fully connected layer, and “softmax” represents the softmax activation function.

The accuracy reached a minimum value close to 50% after 55 and 40 epochs of training with the Gaussian dataset and the channelized dataset, respectively. The results became stable after that. Therefore, the trained generators of epoch 55 and epoch 40 were chosen to perform the following experiments. The semivariogram along the west-east direction was used to show the generative ability of the trained generators:

$$\gamma(h) = \frac{1}{2N(h)} \sum_{i=1}^{N(h)} [f(u_i + h) - f(u_i)]^2 \quad (5)$$

where h is the separation distance, $N(h)$ is the number of pairs of locations, and $f(u_i + h)$ and $f(u_i)$ are the values at point $u_i + h$ and point u_i , respectively. Figure 4 (a) shows the semivariograms after 55 epochs of training for the Gaussian dataset. 2,000 images generated by the trained generator were used to calculate the semivariograms. The mean of semivariograms of the original 2,000 images from the training dataset was used as the reference (red in Figure 4 (a)). The mean of the generated samples is pretty close to the reference. Figure 4 (b) shows the semivariograms for the channelized dataset after 40 epochs of training. The mean of the generated samples matches the reference well. Figure 5 and Figure 6 are randomly chosen training and generated images that illustrate the trained generators can produce realistic images similar to the training images.

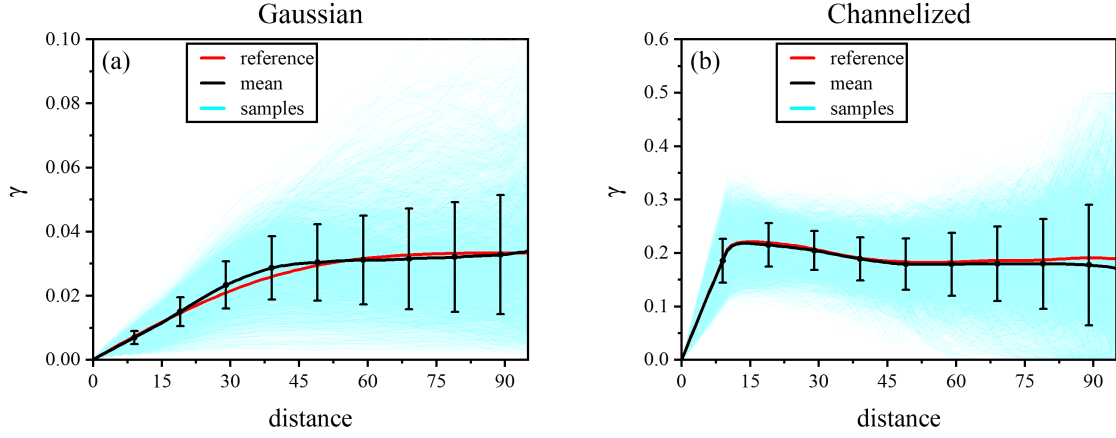


Figure 4. (a) The semivariograms for the Gaussian data; (b) The semivariograms for the channelized data. The red line indicates the reference semivariogram computed from the training images. The blue lines represent the semivariograms of 2,000 generated images. The black line represents the mean, and the error bars indicate the standard deviation of the generated 2,000 samples.

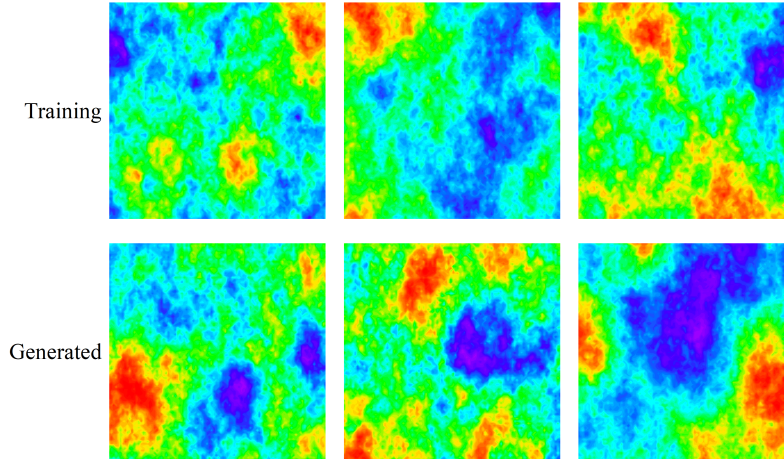


Figure 5. Examples of Gaussian training images (top) and generated images by WGAN-GP (bottom)

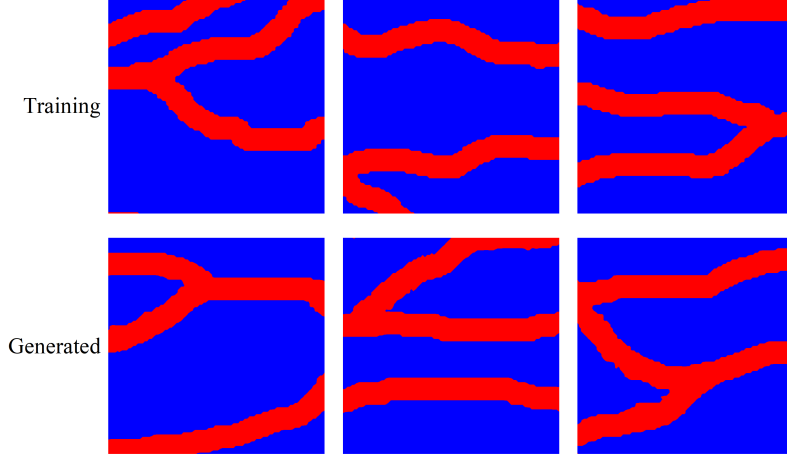


Figure 6. Examples of channelized training images (top) and generated images by WGAN-GP (bottom)

2.2 Ensemble Smoother with Multiple Data Assimilation

Here we follow ES-MDA (A. A. Emerick & Reynolds, 2013) to update the latent space variables \mathbf{z} . We will revisit our choice of ES-MDA for general inverse and data assimilation problems and discuss justifications later. The parameter matrix at the i -th step \mathbf{Z}^i can be expressed as follows:

$$\mathbf{Z}^i = [\mathbf{z}_1^i \quad \mathbf{z}_2^i \quad \cdots \quad \mathbf{z}_{N_r}^i] = \begin{bmatrix} z_{11}^i & z_{12}^i & \cdots & z_{1N_r}^i \\ z_{21}^i & z_{22}^i & \cdots & z_{2N_r}^i \\ \vdots & \vdots & \ddots & \vdots \\ z_{N_d1}^i & z_{N_d2}^i & \cdots & z_{N_dN_r}^i \end{bmatrix} \quad (6)$$

where \mathbf{z}_j^i is j -th realization of the latent space variable vector whose k -th element z_{jk}^i is j -th latent variable in k -th realization where $j = 1, \dots, N_d$ and $k = 1, \dots, N_r$. N_d and N_r represent the number of latent variables and realizations, respectively. In inverse modeling or batch-data assimilation, the forward model can be defined as the following form:

$$\mathbf{d} = F(\mathbf{k}) + \epsilon \quad (7)$$

where \mathbf{d} is the $N_d \times 1$ data vector, such as the hydraulic head at observation locations, $F(\cdot)$ is the forward operator, such as USGS Groundwater Flow Model MODFLOW-2005 (Harbaugh, 2005), \mathbf{k} is the $N_k \times 1$ model parameter vector, and ϵ is the model error. The objective is to estimate the unknown model parameters that reproduce the observation data \mathbf{d}_{obs} , and the updating process in ES-MDA follows the Kalman update through ensemble covariance matrix approximation (Evensen, 1994):

$$\mathbf{z}_j^{i+1} = \mathbf{z}_j^i + \mathbf{C}_{ZD}^i (\mathbf{C}_{DD}^i + \alpha_i \mathbf{C}_D)^{-1} (\mathbf{d}_{uc,j}^i - \mathbf{d}_j^i), \quad j = 1, \dots, N_r \quad (8)$$

where \mathbf{C}_{ZD}^i is the cross-covariance between the latent variables and the simulated data, \mathbf{C}_{DD}^i is the auto-covariance of the simulated data, \mathbf{C}_D is the observation error covariance, and \mathbf{d}_{uc} is the perturbed observation data defined as:

$$\mathbf{d}_{uc} = \mathbf{d}_{obs} + \sqrt{\alpha_i} \mathbf{C}_D^{1/2} \epsilon_d \quad (9)$$

where α_i is the inflation coefficient of the i -th iteration ($\sum_{i=1}^{N_a} \frac{1}{\alpha_i} = 1$, N_a is the number of iterations) and $\epsilon_d \sim N(0, \mathbf{I}_{N_d})$.

In the updating equation 8, the inverse of the auto-covariance matrix $\mathbf{C}_{DD}^i + \alpha_i \mathbf{C}_D$ needs to be computed. However, the matrix may be singular due to the rank N_r ensemble covariance approximation and its small eigenvalues may cause numerical instability and error, thus truncated eigenvalue decomposition is applied to obtain the pseudo-inverse of the auto-covariance matrix, and the measurement error covariance \mathbf{C}_D is rescaled with the Cholesky decomposition $\mathbf{C}_D = \mathbf{C}_D^{1/2} (\mathbf{C}_D^{1/2})^\top$ (A. Emerick, 2012). With the eigenvalue truncation, we obtain

$$\mathbf{C}_{DD}^i + \alpha_i \mathbf{C}_D \approx \mathbf{U}_n \mathbf{\Lambda}_n \mathbf{V}_n^T \quad (10)$$

where $\mathbf{\Lambda}_n$ is a diagonal matrix containing N_n largest eigenvalues. The truncation threshold parameter N_n is defined by the following truncation scheme:

$$\frac{\sum_{i=1}^{N_n} \lambda_i}{\sum_{i=1}^{N_t} \lambda_i} \leq E \quad (11)$$

where λ_i is the i -th singular values sorted in decreasing order, N_t is the total number of singular values, and E is the energy of the eigenvalues retained, typically between 0.9 and 1.0. Thus, N_n is the number that makes the ratio of the sum of the N_n largest singular values to the sum of the total singular values less than or equal to E . The inverse of matrix $\mathbf{C}_{DD}^i + \alpha_i \mathbf{C}_D$ can then be approximated as follows:

$$(\mathbf{C}_{DD}^i + \alpha_i \mathbf{C}_D)^{-1} \approx \mathbf{V}_n \mathbf{\Lambda}_n^{-1} \mathbf{U}_n^T \quad (12)$$

2.3 Coupling WGAN-GP with ES-MDA

Based on the previous developments, we couple WGAN-GP within the ES-MDA framework to characterize spatially distributed hydraulic conductivity fields from sparse datasets. The use of WGAN-GP will encode the data-driven prior distribution and accelerate the estimation of unknown spatial parameters in the encoded, smaller latent space by reducing the computational costs associated with matrix-matrix multiplications, e.g., Jacobian-covariance products (Ghorbanidehno et al., 2020). The procedure of coupling WGAN-GP with ES-MDA is shown in Figure 7. The trained generator is used to map the latent space \mathbf{z} to multiple realizations of the hydraulic conductivity fields from the prior distribution. By simply running “black-box” forward models, the ensemble-based approaches only need to obtain the simulated outputs such as hydraulic heads without the code-intrusive adjoint-state formulation that explicitly constructs Jacobian and its products. ES-MDA updates the latent variables iteratively based on the mismatch between simulated data and observed data until the convergence as shown in Algorithm 1.

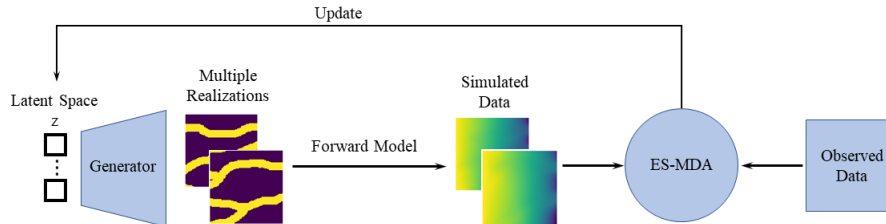


Figure 7. The flowchart of coupling WGAN-GP with ES-MDA.

Algorithm 1: Coupling WGAN-GP with ES-MDA

```

Set:  $N_a$  = The number of iterations
Set:  $\mathbf{d}_{obs}$  = Observed data (e.g., hydraulic head)
Set:  $N_r$  = The number of realizations
begin
  Sample initial  $\mathbf{z}$  from a Gaussian distribution  $N(0, 1)$ 
  for  $i = 1, 2, \dots, N_a$  do
     $\alpha_i = N_a$ 
    for  $j = 1, 2, \dots, N_r$  do
      Generate the hydraulic conductivity fields with the trained generator:
       $\mathbf{K}_j^i = G(\mathbf{z}_j^i)$ 
      Run forward model to obtain the hydraulic head data  $\mathbf{d}_j^i$ 
      Perturb the observation data:  $\mathbf{d}_{uc,j}^i = \mathbf{d}_{obs} + \sqrt{\alpha_i} \mathbf{C}_D^{1/2} \mathbf{I}_d$ 
      Calculate:  $\mathbf{C}_{ZD}^i = \frac{1}{N_r-1} \sum_{j=1}^{N_r} (\mathbf{z}_j^i - \bar{\mathbf{z}}^i)(\mathbf{d}_j^i - \bar{\mathbf{d}}^i)^T$ 
      Calculate:  $\mathbf{C}_{DD}^i = \frac{1}{N_r-1} \sum_{j=1}^{N_r} (\mathbf{d}_j^i - \bar{\mathbf{d}}^i)(\mathbf{d}_j^i - \bar{\mathbf{d}}^i)^T$ 
      Update:  $\mathbf{z}_j^{i+1} = \mathbf{z}_j^i + \mathbf{C}_{ZD}^i (\mathbf{C}_{DD}^i + \alpha_i \mathbf{C}_D)^{-1} (\mathbf{d}_{uc,j}^i - \mathbf{d}_j^i), j = 1, \dots, N_r$ 
    end
  end

```

3 Applications

In this section, two benchmark applications demonstrate the performance of our proposed inversion approach. In the first example, we test with a Gaussian field, where the log-transformed hydraulic conductivity follows a Gaussian distribution. Note that this example can be readily addressed by the traditional inverse modeling methods and their linear dimension reduction variants (Kitanidis, 1995; Lee & Kitanidis, 2014, e.g.,). The second example is a channelized, binary field with two categories: low conductivity areas with high conductivity channels. These benchmark fields are log-transformed and normalized in $[-1, 1]$ for the training purpose. The true fields for Gaussian and channelized fields are randomly selected, neither used for training nor generated by trained generators.

3.1 Gaussian Fields

3.1.1 Model Setup

The true field and model settings are shown in Figure 8 (a). A confined aquifer (480 m \times 480 m \times 10 m) is discretized into 96 rows \times 96 columns \times 1 layer. The logarithmic hydraulic conductivity ranges from -1 to 1 (0.1 m/d to 10 m/d). The northern and southern boundaries are set to no flow boundaries. The western and eastern sides are set to the constant head boundaries with $h = 0$ m and -10 m, respectively. The recharge rate is set to 0.001 m/d. The model is constructed using the USGS groundwater flow model MODFLOW-2005 (Harbaugh, 2005) with its Python interface FloPy (Bakker et al., 2016), and steady-state groundwater flow is simulated for our demonstrations.

3.1.2 Results with Different Observation Layouts

Four cases with different data availability were tested to evaluate the performance of different observation strategies. Figure 8 (b) shows the true field with well locations. Cases 1-3 have 9, 16, and 25 monitoring wells, respectively. The hydraulic tomography (HT) in which we perform cross-well experiments (Gottlieb & Dietrich, 1995; Yeh & Liu, 2000; Lee & Kitanidis, 2014) is applied in Case 4. Case 4 shows an example of a single

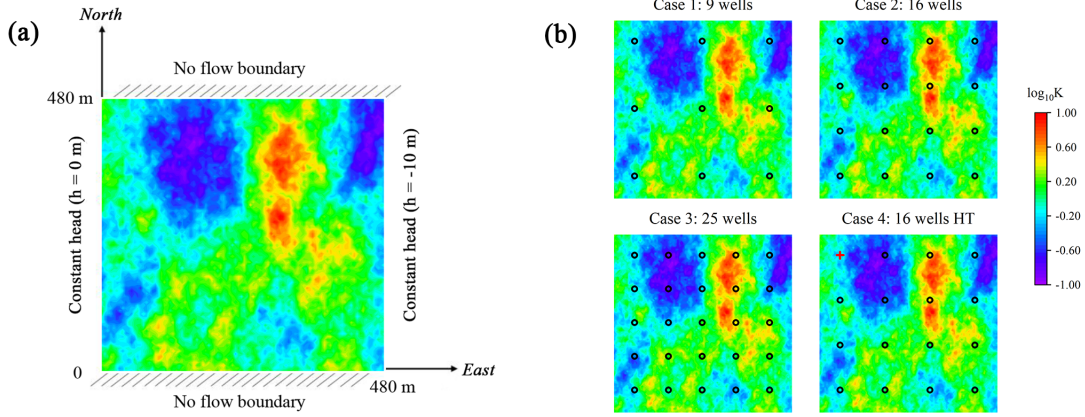


Figure 8. (a) Model settings. No flow on northern and southern boundaries, and constant heads on the western and eastern boundaries are imposed. (b) Well locations for Cases 1-4. Case 4 indicates the hydraulic tomography (HT), and aquifer characterization through multiple cross-well pumping tests. and the red cross represents an example of the pumping location and it moves to the next location once the pumping test is completed. The black circles indicate the locations of monitoring wells.

pumping experiment; the red cross indicates the pumping well location with the pumping rate of $50 \text{ m}^3/\text{d}$ and the black circles represent monitoring wells so that each pumping test produces 15 steady-state head measurements. Once a pumping test is completed, the pumping well moves to the next location and continues the experiment, which results in $16 \text{ (pumping tests)} \times 15 \text{ (measurements/test)} = 240$ measurements in total. A Gaussian error of 0.02 is added to the simulated measurements representing forward modeling and data collection errors.

After hyperparameter calibrations (Kitanidis, 1991), the number of ensembles is set to 200 with the number of maximum iterations to 8. The mean and variance of 200 realizations for different cases are shown in Figure 9. For Cases 1-3, the mean is closer to the true field as more wells are available. Placing more monitoring wells is a straightforward way to improve results at the expense of the well installation and experiment budgets. With HT, we obtain better results with fewer wells as shown in Figure 9 where the result of Case 4 is much better than those from the other cases (see the accuracy reported in Figure 11). We also evaluate the uncertainty of the estimate using the variance computed from the posterior realizations and it is observed that HT reduces uncertainty significantly as expected. Figure 10 shows 3 realizations of Case 4. The proposed approach can reconstruct the main features in the true field, especially with HT.

Figure 11 (a) is a boxplot showing the Root Mean Square Error (RMSE) of the hydraulic conductivity of 200 realizations in each case. RMSE is calculated as follows:

$$RMSE = \sqrt{\frac{1}{N_k} \sum_{i=1}^{N_k} (\mathbf{K}_i - \mathbf{T}_i)^2} \quad (13)$$

where \mathbf{K}_i indicates the estimated parameter value and \mathbf{T}_i is the true value, N_k is the total number of parameters.

It is shown that the mean of the RMSE decreases as more wells are used as expected. The RMSE using HT in Case 4 is much smaller than the other three cases. The spread

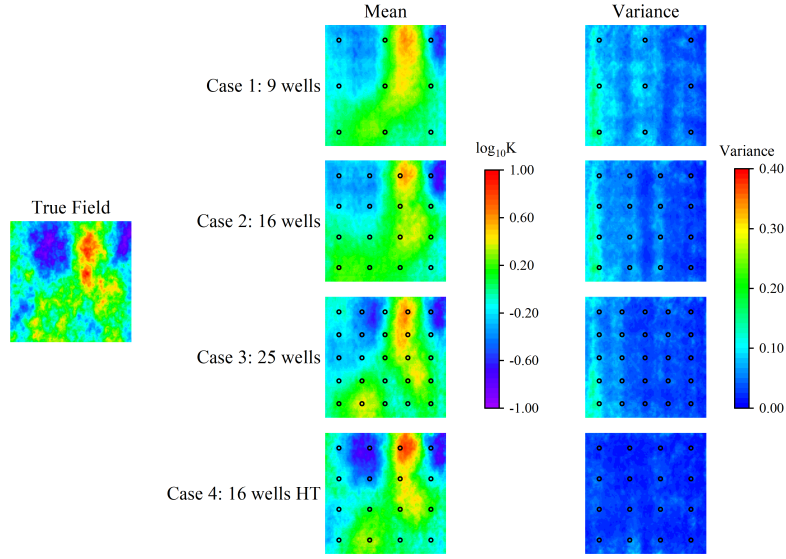


Figure 9. True Field (left), estimated mean (middle), and posterior variance (right) for Gaussian Benchmark Cases. The black circles indicate well locations.

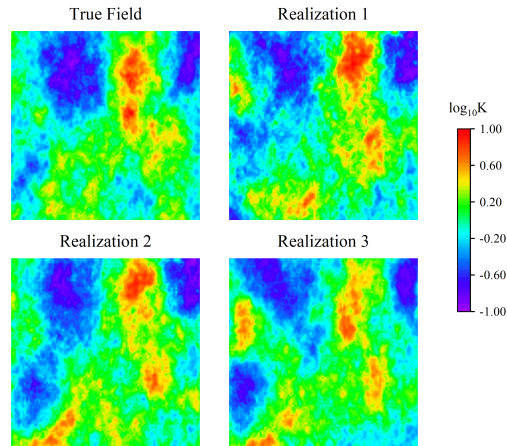


Figure 10. True Gaussian field (top left) and three realizations from the posterior pdf in Case 4.

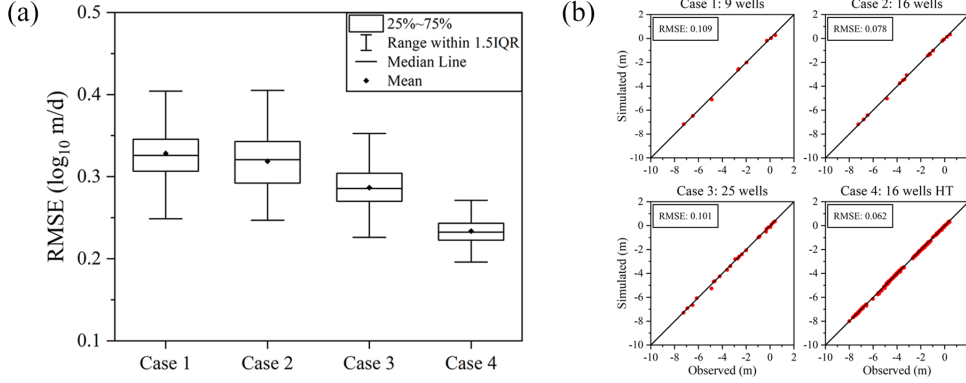


Figure 11. (a) Boxplot of RMSE (\log_{10} m/d) of estimated hydraulic conductivity for Gaussian cases. (b) simulated hydraulic heads vs. observed hydraulic heads for Gaussian cases. The black lines are 45° lines.

in Case 4 is also the smallest, indicating less uncertainty as well as less variability within the conditional realizations. For this Gaussian case, principal component analysis or variational autoencoder-based inversion approaches will work with a similar performance (Lee & Kitanidis, 2014; Forghani et al., 2022).

The fitting error of the simulated hydraulic head and the observed hydraulic head is shown in Figure 11 (b). The red dots indicate the mismatch between observed hydraulic heads and the simulated hydraulic heads, which is the simulation result using estimated mean hydraulic conductivity. The RMSE values are also displayed as an indicator of fitting error in Figure 11 (b). Case 4 has the smallest value, which demonstrates that the inversion results using HT are more accurate as expected.

3.2 Channelized Fields

In this subsection, we tested our proposed method to estimate the subsurface field with high permeable channels, which is more challenging than the previous Gaussian case and the traditional methods would fail to find an accurate solution because of the Gaussian prior assumption (Kadeethum et al., 2021; Kang et al., 2022). Inversion performance was evaluated at various pumping rates and with measurement error levels.

3.2.1 Different Pumping Rates

The true field is shown on the left in Figure 12. The red channels represent connected high conductivity materials such as sand or volcanic lava tubes ($K = 10$ m/d), and the blue areas represent low conductivity materials such as clay ($K = 0.1$ m/d). The black circles indicate well locations. Three cases HT with different pumping rates (10 m³/d, 30 m³/d, and 50 m³/d) were evaluated. A Gaussian error of 0.02 is added to the simulated measurements.

ES-MDA with the same configuration (200 realizations and 8 iterations) is applied to the channelized field characterization. The results are shown in Figure 12 illustrating that data collected at a larger pumping rate leads to an improved result. The mean of 200 realizations becomes closer to the true field as the pumping rate increases. The posterior variance plots reflect (linearized) estimation uncertainty with larger uncertainty around the channel boundaries as expected in the previous research (Lee & Kitanidis, 2013, e.g.) and the variance of the result with 50 m³/d pumping rate is lower than the

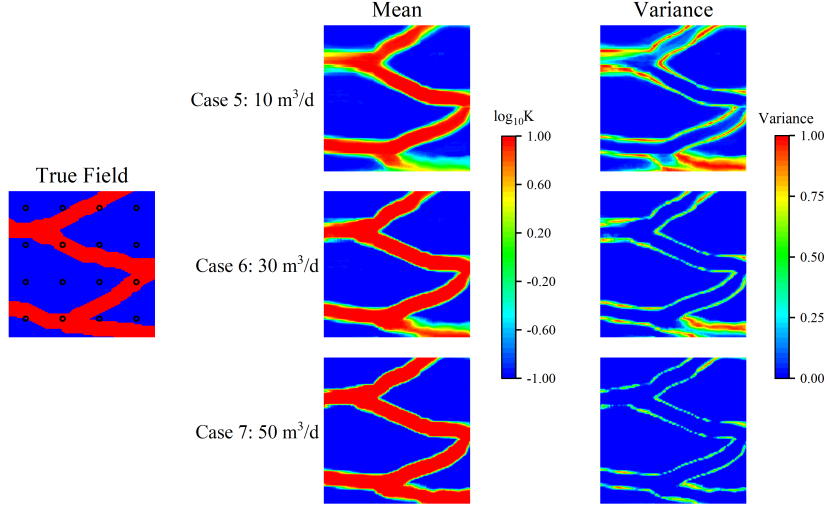


Figure 12. Mean and variance for the channelized field. The true field is shown on the left, and the black circles indicate well locations.

other two cases. Figure 13 (a) also shows the RMSE of estimated hydraulic conductivity for each case confirming the RMSE value decreases dramatically and the uncertainty is significantly reduced as the pumping rate increases. This is expected since the sensitivity of the data, i.e., Jacobian of the forward model $\frac{\partial F}{\partial \mathbf{k}}$, increases as the pumping rate increases, thus the measurement information that contains important features becomes less contaminated by the measurement error (Kitanidis, 1998). Still, the inversion with data at the small pumping rate can identify the structure of underlying channels by incorporating the meaningful data-driven prior from WGAN-GP in the inversion.

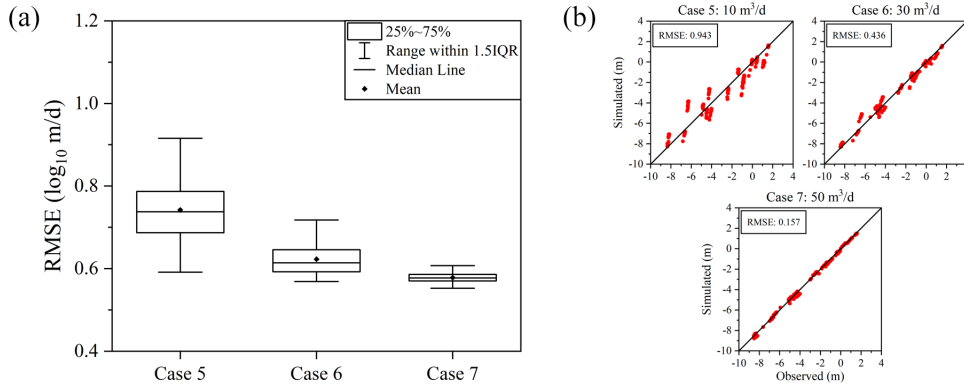


Figure 13. (a) Boxplot of hydraulic conductivity RMSE (\log_{10} m/d) and (b) simulated hydraulic heads vs. observed hydraulic heads for the channelized K cases. The black lines are 45° lines.

The fitting errors with different pumping rates are shown in Figure 13 (b). Like in the Gaussian test cases, the red dots in Figure 13 (b) display the mismatch between the observed hydraulic heads and the simulated hydraulic heads using estimated mean hydraulic conductivity. Note that the mean RMSE values from the smaller pumping rate experiments are larger than the simulated error level of 0.02 because of high variability and uncertainty in the final ensemble that originates from inaccurate estimation around the high permeable channel boundaries as shown in Figure 12.

3.2.2 Different Error Levels

In this subsection, we investigate the performance of the proposed approach under different error levels. As shown in Figure 14, four different error cases were considered in which Gaussian error levels of 0.02, 0.05, 0.2, and 0.5 m are added to the simulated data. The true field and observation layout are also shown in Figure 14. The observed data were obtained from 16 well HT at a pumping rate of 50 m³/d.

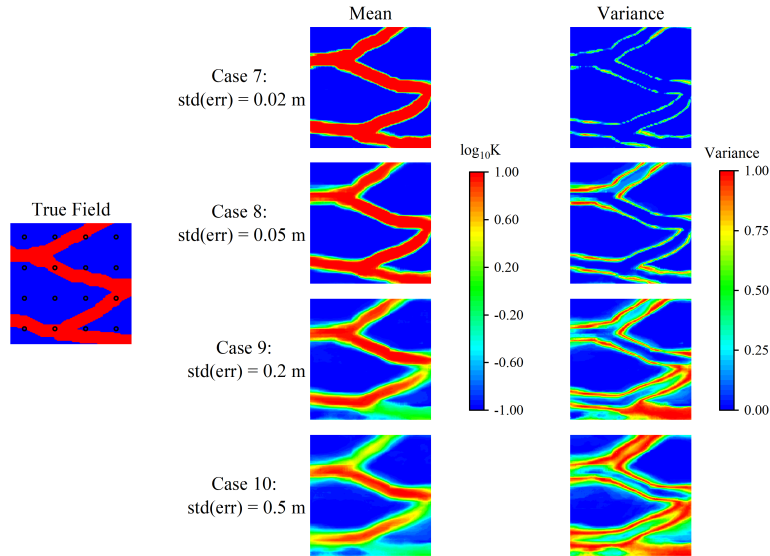


Figure 14. Mean estimates and their posterior variance for different error levels of 0.02, 0.05, 0.2, and 0.5 m, respectively. The true field is shown on the left, and the black circles indicate well locations.

Figure 14 shows the mean estimates and their estimation variance with different error levels. It is observed that our proposed approach can delineate the subsurface features accurately while the estimated hydraulic conductivity fields become blurred around the channel boundaries with larger uncertainty as the noise level increases. Even with the largest error level of 0.5 m, the mean estimate correctly covers the extent of the true high permeable channels. The boxplots in Figure 15 (a) show the RMSE values of estimated hydraulic conductivity for each case. As the error level increases, the RMSE value tends to increase and the RMSE range becomes wider as evidenced in Figure 14. Figure 15 (b) presents the fitting errors of different error levels showing that the estimation is robust to the measurement error level up to 0.05 m in this case.

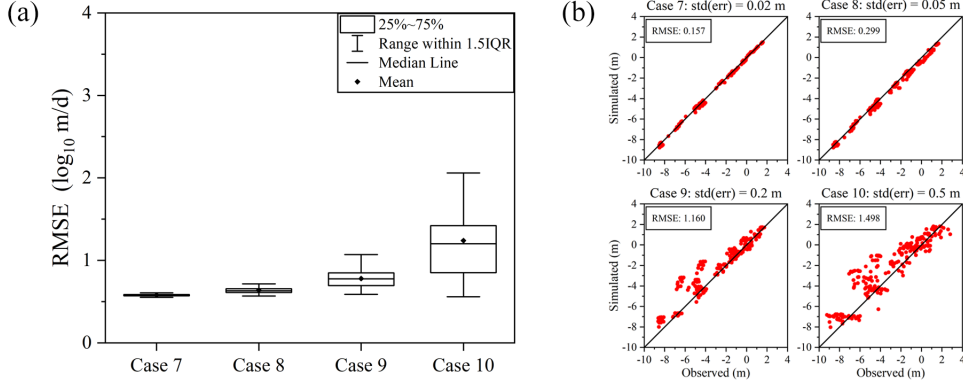


Figure 15. (a) Boxplots of hydraulic conductivity RMSE (\log_{10} m/d) for different error levels. (b) simulated hydraulic heads vs. observed hydraulic heads for different noise levels. The black lines are 45° lines.

4 Discussion

4.1 Non-Gaussianity and Dimension Reduction

The proposed inverse modeling workflow by coupling WGAN-GP with ES-MDA showed satisfactory performance in both Gaussian and channelized test cases. For the Gaussian field, the trained generator plays a role in dimension reduction. The ES-MDA can be applied to the low-dimensional latent space instead of directly working on the high-dimensional hydraulic conductivity field. The 96×96 parameters of the conductivity field are reduced to 6×6 latent variables that need to be updated. For the channelized field, the trained generator plays another role in mapping a Gaussian field to a non-Gaussian field. The ES-MDA only works well for Gaussian distributed variables because of the Gaussian prior assumption, thus is not suitable for the non-Gaussian channelized field. However, the ES-MDA can be applied to the Gaussian distributed latent space using the trained generator, then the generator can produce the non-Gaussian channelized field. This conversion process nicely solves the limitation of ES-MDA or other Gaussian prior-based approaches.

4.2 Compared with Variational Approach

Now, we investigate our choice of the ensemble-based approach, ES-MDA, for our main inversion algorithm over other inverse modeling methods. For this, we perform some experiments using variational inversion (Sasaki, 1958, 1970; Forghani et al., 2022) with WGAN-GP prior to compare with the results using ES-MDA. The code used here for variational inversion implements a Gauss-Newton based optimization with a line search method as in (Forghani et al., 2022). Figures 16 and 17 are the results for the Gaussian and channelized fields, respectively. Both ES-MDA and variational inversion perform well in the Gaussian case as observed in the previous researches (Lee & Kitanidis, 2014; Forghani et al., 2022). However, for the channelized aquifer problem, the variational inversion approach cannot recover the channel structures while ES-MDA can still achieve a good result.

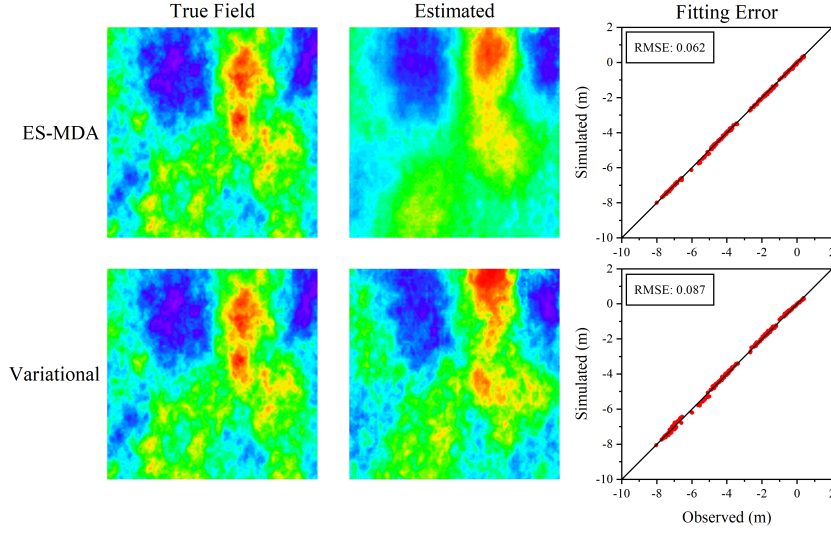


Figure 16. Comparison of the results using ES-MDA and variational inversion for the Gaussian field

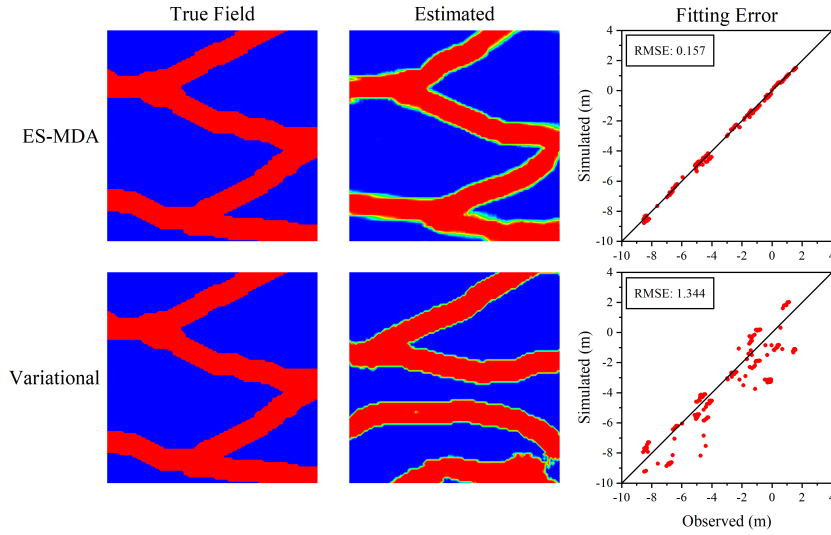


Figure 17. Comparison of the results using ES-MDA and variational inversion for the channelized field

4.3 Regularity of Latent Space

In order to investigate why the ES-MDA method performs better in the channelized case, the objective function L was calculated to visualize the regularity, i.e., roughness, of the latent space:

$$L = \frac{1}{2}(\mathbf{z}_{ref} - \mathbf{z}_{pred})^T \mathbf{C}_Z^{-1}(\mathbf{z}_{ref} - \mathbf{z}_{pred}) + \frac{1}{2}(\mathbf{d}_{obs} - \mathbf{d}_{pred})^T \mathbf{C}_D^{-1}(\mathbf{d}_{obs} - \mathbf{d}_{pred}) \quad (14)$$

where \mathbf{z}_{ref} represents the reference latent values, which are the latent values corresponding to a realization that is close to the true field as in Figure 9 and Figure 12. \mathbf{z}_{pred} represents the predicted latent values for each iteration of the data assimilation or the inversion process. \mathbf{C}_Z is the latent error matrix. By the construction of the latent variables following the Gaussian distribution $N(0, 1)$, thus the diagonal entries of \mathbf{C}_Z and \mathbf{C}_Z^{-1} are 1. \mathbf{d}_{obs} is the observed data, \mathbf{d}_{pred} is the predicted data, and \mathbf{C}_D is the observed error matrix. We assume the observed error follows the Gaussian distribution $N(0, 0.02^2)$, thus the diagonal entries of \mathbf{C}_D^{-1} are $1/(0.02^2) = 2,500$. Both variational inversion and ES-MDA minimize the same objective function 14, however, their minimization approaches are different; the variational inversion directly applies the Gauss-Newton method (Nocedal & Wright, 2006) to the objective function (Eq. 14) while the ensemble-based approach approximates the covariance matrices in the objective function by an ensemble or generated samples and then perform the optimization by minimizing their expected objective function value (Anderson, 2003; Lee et al., 2018). It is shown that the accurate covariance approximation from an ensemble requires a number of generated realizations (Johnstone, 2001; El Karoui, 2008), which is generally regarded as a limitation of the ensemble-based inversion since it makes the objective function space smooth and leads to a suboptimal solution (Lee et al., 2018). However, for the applications presented in this study, this ensemble-based approximation error actually regularizes the problem in a beneficial way and provides better solutions.

Figure 18 shows an example of objective functions with respect to \mathbf{z}_3 and \mathbf{z}_4 for the Gaussian and channelized cases, where \mathbf{z}_i is the i -th latent space variable. We chose third and fourth latent variables \mathbf{z}_3 and \mathbf{z}_4 for effective illustration but the patterns of the 9 (3×3) latent variables are similar. \mathbf{z}_3 and \mathbf{z}_4 are sampled from $[-5, 5]$ with an interval of 0.1. The channelized space is pretty rough due to the nonlinear, aggressive (96×96 to 3×3) dimension reduction, while the Gaussian space is much smoother and suitable for the Gauss-Newton type methods as expected (Lee & Kitanidis, 2014). The third and fourth columns in Figure 18 are the 1D plots near the reference values of \mathbf{z}_3 and \mathbf{z}_4 . For the Gaussian case, the minimum values are clearly shown in the plots. However, the channelized case has several local minima, which may hinder the algorithms from finding the global minima unless one carefully applies non-smooth function optimization techniques (Hiriart-Urruty & Lemaréchal, 1993; Nocedal & Wright, 2006).

Figure 19 shows the Gauss-Newton update paths of variational inversion and ES-MDA. For the Gaussian case, both methods can reach some points close to the reference (i.e., optimal) values. For the channelized case, however, variational inversion is more likely to get stuck in some local minima, while ES-MDA can identify the correct optimization paths to the global minimum through an average gradient for the ensemble (Anderson, 2003). Variational inversion here implemented the Gauss-Newton method with simple line search (Forghani et al., 2022) and Levenberg–Marquardt algorithms (Nowak & Cirpka, 2004) but still could not handle the non-linearity. For non-smooth functions as in the channelized case, it is easy to converge into local minima as in Figure 19. ES-MDA updates multiple realizations at the same time and the expected Gauss-Newton update step at each iteration is determined by the average of individual update in each realization. Such strategy can select feasible minimization directions and effectively make the objec-

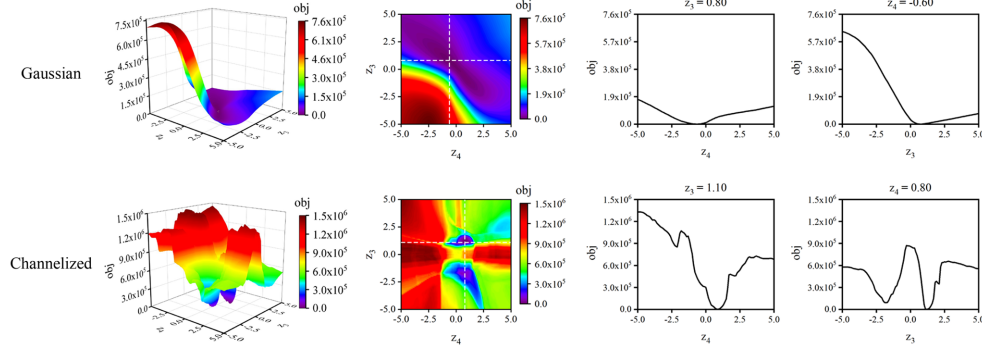


Figure 18. Objective functions with respect to \mathbf{z}_3 and \mathbf{z}_4 . The first row is the Gaussian case, and the second row is the channelized case. The first and second columns are the 3D and 2D plots of the objective functions. The third and fourth columns are the plots near the reference values of \mathbf{z}_3 and \mathbf{z}_4 . The white lines in the second column indicate the locations of the plots.

tive function surface smooth for better convergence at the cost of more function evaluations.

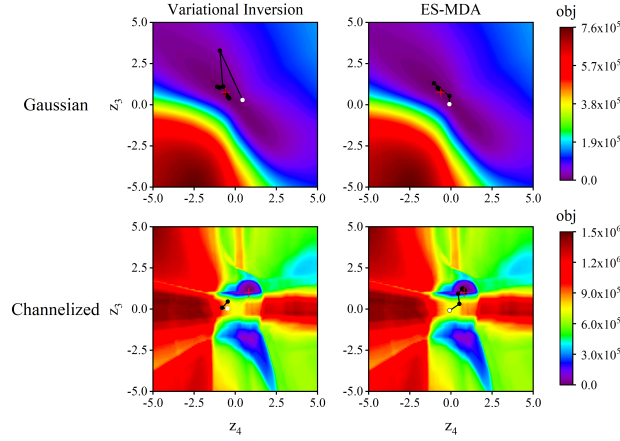


Figure 19. Update paths with respect to \mathbf{z}_3 and \mathbf{z}_4 . The first column shows the results using variational inversion for the Gaussian and channelized cases. The second column shows the results using ES-MDA, only the mean of 200 realizations is shown here. Red crosses indicate reference values, white dots indicate starting points, and black dots represent predicted values.

4.4 Fractured Field Application

In this section, a fractured field was tested to demonstrate the application of the proposed approach for another difficult inverse problem: discrete fractured media or local-scale high-permeable inclusions. 80,000 images with randomly generated fractures were used for training. The fractures have 3 orientations: 0° , 45° , and 90° . The fractures are 10 to 20 pixels long and 2 pixels wide. The network architecture is the same as in the channelized case (Table 2). To show the performance comparison clearly, we select an image generated by the trained generator as the true field for experiments. The model

settings including boundary conditions and well configurations are the same as shown in Figure 8, and the estimation results are shown in Figure 20. To visualize the estimated fractures clearer, we applied a threshold of 0.2 for final binary image production. All the fractures have a log-conductivity of 1 (\log_{10} in m/d as white fractures in Figure 20), and the background matrix has a log-conductivity of -1 (\log_{10} in m/d as background black domain in Figure 20). As expected, the ES-MDA method performs better than the variational approach by reconstructing most of fracture features and reproducing the observations with a much smaller RMSE value of 0.217 m.

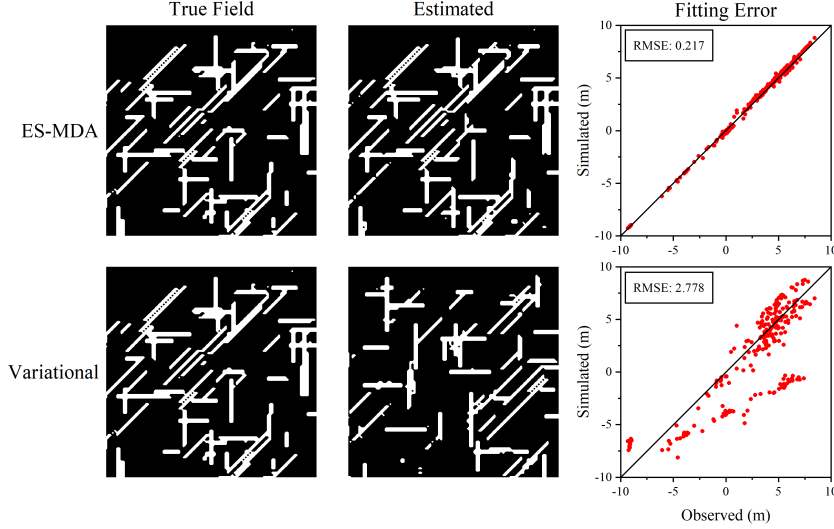


Figure 20. Comparison of the results using ES-MDA and variational inversion for the fractured field

4.5 Extrapolation Capability of WGAN-GP/ES-MDA Inversion Framework

Lastly, we test the estimation accuracy of our inversion framework with a true field beyond the generation capability of WGAN-GP. For this, we intentionally select one of the test data as the true field that is most far away from realizations generated from WGAN-GP and perform the inversion with the observations from the true field as shown in Field 2 of Figure 21). For the comparison purpose, we plot the result of Case 7 from the previous section for a true K field that is randomly chosen from the test data set (Field 1 in Figure 21). As shown in Figure 21, the results of the Field 2 case are worse than those from the Field 1 case simply because the trained generative model does not have the power to reproduce Field 2, especially connected structures near the domain boundaries. As a result, the mean estimate of the Field 2 estimation is more blurry with the channel shapes slightly shifted from the true field. Field 1 has a fitting error of RMSE 0.157 m and Field 2 has a much larger fitting error of RMSE 0.438 m. Still, the proposed framework carries out the right inversion task within its generation capability and estimates the field as close to the true field as possible. This indicates a potentially superior extrapolation capability of our proposed work especially when the deep generative model misses important subsurface features in the aquifer.

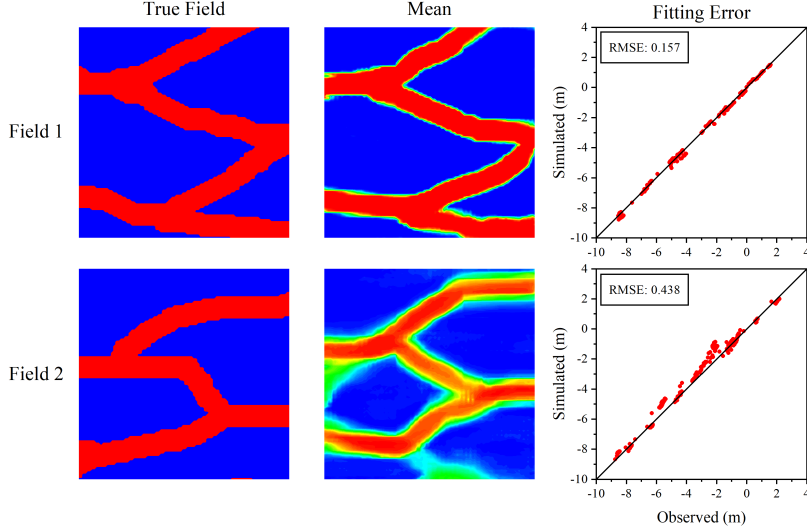


Figure 21. Comparison of different true fields.

5 Conclusion

In this work, a data assimilation/inversion workflow coupling Wasserstein generative adversarial network with gradient penalty (WGAN-GP) with ensemble smoother with multiple data assimilation (ES-MDA) is proposed for accurate and scalable subsurface characterization. WGAN-GP addresses the limitations of adversarial generative models such as mode collapse and ensures an accurate representation of underlying complex spatial fields. ES-MDA is intended to search for an optimal inverse solution without introducing user-controlled optimization parameters.

The trained generators of WGAN-GP were used to reparameterize high-dimensional conductivity fields with low-dimensional latent spaces and ES-MDA was then used to update the latent variables. Through this coupling, the non-Gaussian fields can be mapped to a Gaussian distributed space via WGAN-GP, which allows ES-MDA to work properly with its internal Gaussian assumption. We applied the proposed method to several test cases that aim to identify unknown Gaussian, channelized, and fractured hydraulic conductivity fields from sparse data sets. The numerical experiments show that the 96×96 parameters of the conductivity fields can be reduced to 6×6 (Gaussian case) and 3×3 (channelized and fractured cases) latent variables. The results illustrate: (1) coupling WGAN-GP with ES-MDA can reconstruct the main features of the Gaussian field as expected and accurately estimate the complex small-scale features in the channelized and fractured fields; (2) the proposed method can accommodate more information and accordingly improve the estimation results with lower uncertainty, for example, by installing more observation wells, cross-well pumping tests such as hydraulic tomography with fewer wells, and/or geophysical sensing data; (3) the proposed approach is robust to the data contaminated with high errors (e.g., $\text{std}(\text{err}) = 0.2 \text{ std}$ and 0.5 m) and the mean estimate can still identify the main underlying complex features with reasonable uncertainty quantification.

One of the main contributions of this paper is to justify the use of ensemble-based approaches when using deep generative models. Moreover, the proposed approach outperforms variational inversion for minimizing non-smooth, multimodal objective func-

tions as shown in the channelized and fractured cases. It is observed that multiple realizations examined in the proposed method lead to easier objective function minimization with prudent Gauss-Newton steps, thus the proposed method is less likely to get stuck in local minima and can converge to the close-to-optimal inverse solution with better estimation accuracy. However, the variational approach can reduce the number of forward model runs up to the latent variable dimension, for example, about 10 forward model runs at each iteration. Additional development and modification are needed for the variational inversion approach that ensures local and global convergence using robust techniques such as Trust-region methods (Boyd & Vandenberghe, 2004; Nocedal & Wright, 2006).

The proposed approach is also computationally efficient, and it is easy to apply parallelization. The data assimilation process takes around 7 minutes with 200 realizations and 8 iterations on a workstation with 64G RAM Intel(R) Core(TM) i9-9900X CPU @ 3.50GHz. The coupled WGAN-GP/ES-MDA python code used in this paper can be found in the <https://github.com/jichao1/WGAN-GP.git>.

Acknowledgments

This work is supported by the US Department of Energy Office of Fossil Energy and Carbon Management project - Science-Informed Machine Learning to Accelerate Real-Time Decisions in Subsurface Applications (SMART) initiative. Sandia National Laboratories is a multi-mission laboratory managed and operated by National Technology & Engineering Solutions of Sandia, LLC (NTESS), a wholly owned subsidiary of Honeywell International Inc., for the U.S. Department of Energy’s National Nuclear Security Administration (DOE/NNSA) under contract DE-NA0003525. This written work is authored by an employee of NTESS. The employee, not NTESS, owns the right, title, and interest in and to the written work and is responsible for its contents. Any subjective views or opinions that might be expressed in the written work do not necessarily represent the views of the U.S. Government. The publisher acknowledges that the U.S. Government retains a non-exclusive, paid-up, irrevocable, world-wide license to publish or reproduce the published form of this written work or allow others to do so, for U.S. Government purposes. The DOE will provide public access to results of federally sponsored research in accordance with the DOE Public Access Plan.

References

- Anderson, J. L. (2003). A local least squares framework for ensemble filtering. *Monthly Weather Review*, 131(4), 634–642.
- Arjovsky, M., Chintala, S., & Bottou, L. (2017). Wasserstein generative adversarial networks. In *International conference on machine learning* (pp. 214–223).
- Bakker, M., Post, V., Langevin, C. D., Hughes, J. D., White, J. T., Starn, J., & Fienen, M. N. (2016). Scripting modflow model development using python and flopy. *Groundwater*, 54(5), 733–739.
- Berthelot, D., Schumm, T., & Metz, L. (2017). Began: Boundary equilibrium generative adversarial networks. *arXiv preprint arXiv:1703.10717*.
- Boyd, S., & Vandenberghe, L. (2004). *Convex optimization*. Cambridge University Press.
- Carrassi, A., Bocquet, M., Bertino, L., & Evensen, G. (2018). Data assimilation in the geosciences: An overview of methods, issues, and perspectives. *Wiley Interdisciplinary Reviews: Climate Change*, 9(5), e535.
- Chen, Y., & Oliver, D. S. (2012). Ensemble randomized maximum likelihood method as an iterative ensemble smoother. *Mathematical Geosciences*, 44(1), 1–26.
- Chen, Y., & Zhang, D. (2006). Data assimilation for transient flow in geologic formations via ensemble Kalman filter. *Advances in Water Resources*, 29(8), 1107–1122.

- Creswell, A., White, T., Dumoulin, V., Arulkumaran, K., Sengupta, B., & Bharath, A. A. (2018). Generative adversarial networks: An overview. *IEEE Signal Processing Magazine*, 35(1), 53–65.
- El Karoui, N. (2008, 12). Spectrum estimation for large dimensional covariance matrices using random matrix theory. *Annals of Statistics*, 36(6), 2757–2790.
- Emerick, A. (2012). *History matching and uncertainty characterization: Using ensemble-based methods*. LAP LAMBERT Academic Publishing.
- Emerick, A. A. (2016). Analysis of the performance of ensemble-based assimilation of production and seismic data. *Journal of Petroleum Science and Engineering*, 139, 219–239.
- Emerick, A. A., & Reynolds, A. C. (2013). Ensemble smoother with multiple data assimilation. *Computers & Geosciences*, 55, 3–15.
- Evensen, G. (1994). Sequential data assimilation with a nonlinear quasi-geostrophic model using Monte Carlo methods to forecast error statistics. *Journal of Geophysical Research: Oceans*, 99(C5), 10143–10162.
- Fokker, P., Wassing, B., Van Leijen, F., Hanssen, R., & Nieuwland, D. (2016). Application of an ensemble smoother with multiple data assimilation to the bergermeer gas field, using ps-insar. *Geomechanics for Energy and the Environment*, 5, 16–28.
- Forghani, M., Qian, Y., Lee, J., Farthing, M., Hesser, T., Kitanidis, P. K., & Darve, E. F. (2022). Variational encoder geostatistical analysis (vegas) with an application to large scale riverine bathymetry. *Advances in Water Resources*, 170, 104323.
- Ghorbanidehno, H., Kokkinaki, A., Lee, J., & Darve, E. (2020). Recent developments in fast and scalable inverse modeling and data assimilation methods in hydrology. *Journal of Hydrology*, 591, 125266.
- Gómez-Hernández, J. J., & Journel, A. G. (1993). Joint sequential simulation of multigaussian fields. In *Geostatistics troia'92* (pp. 85–94). Springer.
- Goodfellow, I., Pouget-Abadie, J., Mirza, M., Xu, B., Warde-Farley, D., Ozair, S., ... Bengio, Y. (2014). Generative adversarial nets. In *Advances in neural information processing systems* (pp. 2672–2680).
- Gottlieb, J., & Dietrich, P. (1995). Identification of the permeability distribution in soil by hydraulic tomography. *Inverse Problems*, 11(2), 353.
- Grover, A., Dhar, M., & Ermon, S. (2018). Flow-gan: Combining maximum likelihood and adversarial learning in generative models. In *Proceedings of the aaai conference on artificial intelligence* (Vol. 32).
- Gu, Y., & Oliver, D. (2007). An iterative ensemble kalman filter for multiphase fluid flow data assimilation. *SPE Journal*, 12(4), 438–446.
- Gulrajani, I., Ahmed, F., Arjovsky, M., Dumoulin, V., & Courville, A. C. (2017). Improved training of wasserstein gans. *Advances in neural information processing systems*, 30.
- Harbaugh, A. W. (2005). *Modflow-2005, the us geological survey modular ground-water model: the ground-water flow process*. US Department of the Interior, US Geological Survey Reston, VA, USA.
- He, K., Zhang, X., Ren, S., & Sun, J. (2016). Deep residual learning for image recognition. In *Proceedings of the ieee conference on computer vision and pattern recognition* (pp. 770–778).
- Hiriart-Urruty, J.-B., & Lemaréchal, C. (1993). *Convex analysis and minimization algorithms i: Fundamentals* (Vol. 305). Springer science & business media.
- Hu, L. Y. (2000). Gradual deformation and iterative calibration of gaussian-related stochastic models. *Mathematical Geology*, 32(1), 87–108.
- Janssens, N., Huysmans, M., & Swennen, R. (2020). Computed tomography 3d super-resolution with generative adversarial neural networks: Implications on unsaturated and two-phase fluid flow. *Materials*, 13(6), 1397.

- Johnstone, I. M. (2001). On the distribution of the largest eigenvalue in principal components analysis. *Annals of statistics*, 295–327.
- Kadeethum, T., O'Malley, D., Choi, Y., Viswanathan, H. S., Bouklas, N., & Yoon, H. (2022). Continuous conditional generative adversarial networks for data-driven solutions of poroelasticity with heterogeneous material properties. *Computers & Geosciences*, 167, 105212.
- Kadeethum, T., O'Malley, D., Fuhg, J. N., Choi, Y., Lee, J., Viswanathan, H. S., & Bouklas, N. (2021). A framework for data-driven solution and parameter estimation of pdes using conditional generative adversarial networks. *Nature Computational Science*, 1(12), 819–829.
- Kang, X., Kokkinaki, A., Kitanidis, P. K., Shi, X., Lee, J., Mo, S., & Wu, J. (2021). Hydrogeophysical characterization of nonstationary dnapi source zones by integrating a convolutional variational autoencoder and ensemble smoother. *Water Resources Research*, 57(2), e2020WR028538.
- Kang, X., Kokkinaki, A., Kitanidis, P. K., Shi, X., Revil, A., Lee, J., . . . Wu, J. (2020). Improved characterization of dnapi source zones via sequential hydrogeophysical inversion of hydraulic-head, self-potential and partitioning tracer data. *Water Resources Research*, 56(8), e2020WR027627.
- Kang, X., Kokkinaki, A., Shi, X., Yoon, H., Lee, J., Kitanidis, P. K., & Wu, J. (2022). Integration of deep learning-based inversion and upscaled mass-transfer model for dnapi mass-discharge estimation and uncertainty assessment. *Water Resources Research*, 58(10), e2022WR033277.
- Kitanidis, P. K. (1991). Orthonormal residuals in geostatistics: Model criticism and parameter estimation. *Mathematical Geology*, 23(5), 741–758.
- Kitanidis, P. K. (1995). Quasi-linear geostatistical theory for inversing. *Water resources research*, 31(10), 2411–2419.
- Kitanidis, P. K. (1998). How observations and structure affect the geostatistical solution to the steady-state inverse problem. *Groundwater*, 36(5), 754–763.
- Laloy, E., Héroult, R., Jacques, D., & Linde, N. (2018). Training-image based geostatistical inversion using a spatial generative adversarial neural network. *Water Resources Research*, 54(1), 381–406.
- Le, D. H., Younis, R., Reynolds, A. C., et al. (2015). A history matching procedure for non-gaussian facies based on es-mds. In *Spe reservoir simulation symposium*.
- Lee, J., Ghorbanidehno, H., Farthing, M. W., Hesser, T. J., Darve, E. F., & Kitanidis, P. K. (2018). Riverine bathymetry imaging with indirect observations. *Water Resources Research*, 54(5), 3704–3727.
- Lee, J., & Kitanidis, P. (2013). Bayesian inversion with total variation prior for discrete geologic structure identification. *Water Resources Research*, 49(11), 7658–7669.
- Lee, J., & Kitanidis, P. K. (2014). Large-scale hydraulic tomography and joint inversion of head and tracer data using the principal component geostatistical approach (pcga). *Water Resources Research*, 50(7), 5410–5427.
- Li, L., Zhou, H., Gómez-Hernández, J. J., & Franssen, H.-J. H. (2012). Jointly mapping hydraulic conductivity and porosity by assimilating concentration data via ensemble Kalman filter. *Journal of Hydrology*, 428, 152–169.
- Liu, G., Chen, Y., & Zhang, D. (2008). Investigation of flow and transport processes at the made site using ensemble kalman filter. *Advances in Water Resources*, 31(7), 975–986.
- Liu, Y., & Gupta, H. V. (2007). Uncertainty in hydrologic modeling: Toward an integrated data assimilation framework. *Water resources research*, 43(7).
- Liu, Y., Weerts, A., Clark, M., Hendricks Franssen, H.-J., Kumar, S., Moradkhani, H., . . . others (2012). Advancing data assimilation in operational hydrologic forecasting: progresses, challenges, and emerging opportunities. *Hydrology and Earth System Sciences*, 16(10), 3863–3887.

- Lopez-Paz, D., & Oquab, M. (2016). Revisiting classifier two-sample tests. *arXiv preprint arXiv:1610.06545*.
- Mao, X., Li, Q., Xie, H., Lau, R. Y., Wang, Z., & Paul Smolley, S. (2017). Least squares generative adversarial networks. In *Proceedings of the IEEE international conference on computer vision* (pp. 2794–2802).
- Newell, P., Yoon, H., Martinez, M., Bishop, J., & Bryant, S. (2017). Investigation of the influence of geomechanical and hydrogeological properties on surface uplift at in salah. *Journal of Petroleum Science and Engineering*, 155, 34–45.
- Nocedal, J., & Wright, S. J. (2006). *Numerical optimization* (2nd ed.) [Book]. New York: Springer.
- Nowak, W., & Cirpka, O. A. (2004). A modified levenberg–marquardt algorithm for quasi-linear geostatistical inversing. *Advances in water resources*, 27(7), 737–750.
- Nowozin, S., Cseke, B., & Tomioka, R. (2016). f-gan: Training generative neural samplers using variational divergence minimization. *Advances in neural information processing systems*, 29.
- Oliver, D. S., Cunha, L. B., & Reynolds, A. C. (1997). Markov chain monte carlo methods for conditioning a permeability field to pressure data. *Mathematical Geology*, 29(1), 61–91.
- O’Searcoid, M. (2006). *Metric spaces*. Springer Science & Business Media.
- Paszke, A., Gross, S., Massa, F., Lerer, A., Bradbury, J., Chanan, G., ... others (2019). Pytorch: An imperative style, high-performance deep learning library. *Advances in neural information processing systems*, 32, 8026–8037.
- Patel, D. V., & Oberai, A. A. (2021). Gan-based priors for quantifying uncertainty in supervised learning. *SIAM/ASA Journal on Uncertainty Quantification*, 9(3), 1314–1343.
- Remy, N., Boucher, A., & Wu, J. (2009). *Applied geostatistics with sgems: A user’s guide*. Cambridge University Press.
- Sasaki, Y. (1958). An objective analysis based on the variational method. *Journal of the Meteorological Society of Japan. Ser. II*, 36(3), 77–88.
- Sasaki, Y. (1970). Some basic formalisms in numerical variational analysis. *Monthly Weather Review*, 98(12), 875–883.
- Sun, A. Y. (2018). Discovering state-parameter mappings in subsurface models using generative adversarial networks. *Geophysical Research Letters*, 45(20), 11–137.
- Tartakovsky, D. M. (2013). Assessment and management of risk in subsurface hydrology: A review and perspective. *Advances in Water Resources*, 51, 247–260.
- Tavakoli, R., Yoon, H., Delshad, M., ElSheikh, A. H., Wheeler, M. F., & Arnold, B. W. (2013). Comparison of ensemble filtering algorithms and null-space monte carlo for parameter estimation and uncertainty quantification using co2 sequestration data. *Water Resources Research*, 49(12), 8108–8127.
- Turhan, C. G., & Bilge, H. S. (2018). Recent trends in deep generative models: a review. In *2018 3rd international conference on computer science and engineering (ubmk)* (pp. 574–579).
- Van Leeuwen, P. J., & Evensen, G. (1996). Data assimilation and inverse methods in terms of a probabilistic formulation. *Monthly Weather Review*, 124(12), 2898–2913.
- Villani, C. (2009). *Optimal transport: old and new* (Vol. 338). Springer.
- Wang, R., Chen, C., Lee, J., & Darve, E. (2021). Pbbfmm3d: a parallel black-box algorithm for kernel matrix-vector multiplication. *Journal of Parallel and Distributed Computing*, 154, 64–73.
- Xu, Q., Huang, G., Yuan, Y., Guo, C., Sun, Y., Wu, F., & Weinberger, K. (2018). An empirical study on evaluation metrics of generative adversarial networks. *arXiv preprint arXiv:1806.07755*.

- Yeh, T.-C. J., & Liu, S. (2000). Hydraulic tomography: Development of a new aquifer test method. *Water Resources Research*, 36(8), 2095–2105.
- Yoon, H., Hart, D. B., & McKenna, S. A. (2013). Parameter estimation and predictive uncertainty in stochastic inverse modeling of groundwater flow: Comparing null-space monte carlo and multiple starting point methods. *Water Resources Research*, 49(1), 536–553.
- Zhang, J., Lin, G., Li, W., Wu, L., & Zeng, L. (2018). An iterative local updating ensemble smoother for estimation and uncertainty assessment of hydrologic model parameters with multimodal distributions. *Water Resources Research*, 54(3), 1716–1733.
- Zhao, J., Mathieu, M., & LeCun, Y. (2016). Energy-based generative adversarial network. *arXiv preprint arXiv:1609.03126*.
- Zhou, H., Gómez-Hernández, J. J., & Li, L. (2014). Inverse methods in hydrogeology: Evolution and recent trends. *Advances in Water Resources*, 63, 22–37.